Enhancing the cycling stability of a hollow architecture Li-rich cathode *via* Ce-integrated surface/interface/doping engineering†

Zhaozhe Yu,[a] Kangzhe Yu,[a] Fangli Ji,[b] Quan Lu,[a] Yuezhen Wang,[a] Yan Cheng, [ID] *[a] Huacheng Li,[a] Fen Xu, [ID] [a] Lixian Sun, [ID] *[a] Hans J. Seifert,[c] Yong Du[d] and Jianchuan Wang [ID] [d]

Li-rich Mn-based cathode materials possess a high specific capacity, but their application is hindered by their inherent anion activity and surface instability. Herein, we propose the design of a spinel heterogeneous interface with oxygen buffering effects in the $Li_{1.2}Mn_{0.6}Ni_{0.2}O_2$ hollow architecture by Ce intervention. The hollow architecture shortens the Li-ion diffusion paths. Ce intervention induces the spinel phase formed on the subsurface, and then constructs a phase boundary to restrain the outward migration of bulk oxygen anions and promote charge transfer. The formed $LiCeO_2$ coating layer with oxygen vacancies accelerates the diffusion of Li ions and decelerates electrolyte corrosion. Moreover, Ce doping in the bulk phase effectually stabilizes the evolution of lattice oxygen and suppresses the structural deformation. The prepared $Li_{1.2}Mn_{0.6}Ni_{0.2}Ce_xO_{2-y}$–$LiCeO_2$ (LLO@Ce−LCO) cathode exhibits a remarkable reversible capacity (267.3 mA h g^{-1} at 20 mA g^{-1}) and great cycling stability (capacity retention of about 86% after 200 cycles at 200 mA g^{-1}). This hollow architecture and spinel heterogeneous interface strategy provide a novel approach for achieving high-performance cathode materials.

1. Introduction

With the increasing demand for lithium-ion batteries (LIBs) to drive pure/hybrid electric vehicles, the development of high-energy-density cathode materials has received considerable attention.[1,2] Lithium-rich layered oxide materials (LLOs), Li_2MnO_3–$LiMO_2$ (M = Mn, Ni, Co), have been regarded as promising candidates for next generation LIBs with a high energy density owing to their extraordinarily high capacity, usually exceeding 250 mA h g^{-1}.[3–5] Such a high capacity is ascribed to the additional capacity that originated from the activation of Li_2MnO_3 during the first charging process.[6–8] However, the activation process of LLOs always brings irreversible Li$^+$ extraction, oxygen release and transition ion migration, leading to structural evolution from the layered to the spinel phase and then severe voltage/capacity fading. These drawbacks hinder LLO applications.[9–11]

Several research studies verified that surface modification and bulk doping could realize performance improvements in LLOs. Surface coating can stabilize the crystal structure and suppress surface corrosion to control the capacity decay of LLOs during the cycle.[12–14] However, most coating layers do not match the lattice structure of LLOs, which leads to the integration structure with nonuniform coating and broken stability during the cycle.[15–17] On the other hand, although bulk doping with different elements and introducing oxygen vacancies into LLOs have good effects on improving the structural stability and reducing the oxygen release, this remedy cannot effectively avoid HF corrosion during the charge/discharge processes.[18–23] Therefore, a onefold modification strategy cannot afford to address all the challenges encountered by LLOs; however, the combined application of multiple modifications is considered to be the most effective solution. For example, Peng and co-workers prepared an LLO cathode with F-doping and surface coating of the oxygen vacancies bearing CeO_2, achieving a discharge capacity of 287.4 mA h g^{-1} at 0.2C and 211.3 mA h g^{-1} at 2C and good cycling stability.[24] However, this modification method is complex and it is difficult to control the balance between the coating and the doping content. In addition, some researchers have attempted

[a]*Engineering Research Center of Electronic Information Materials and Devices, Ministry of Education, Guilin University of Electronic Technology, Guilin 541004, P. R. China. E-mail: chengyan1018@guet.edu.cn, sunlx@guet.edu.cn*

[b]*Guangxi CNGR New Energy Science & Technology Co., Ltd., Qinzhou 535000, P. R. China*

[c]*Karlsruhe Institute of Technology, Institute for Applied Materials – Applied Materials Physics, Hermann-von-Helmholtz-Platz 1, 76344 Eggenstein-Leopoldshafen, Germany*

[d]*State Key Laboratory of Powder Metallurgy, Central South University, Changsha, Hunan, 410083, China*
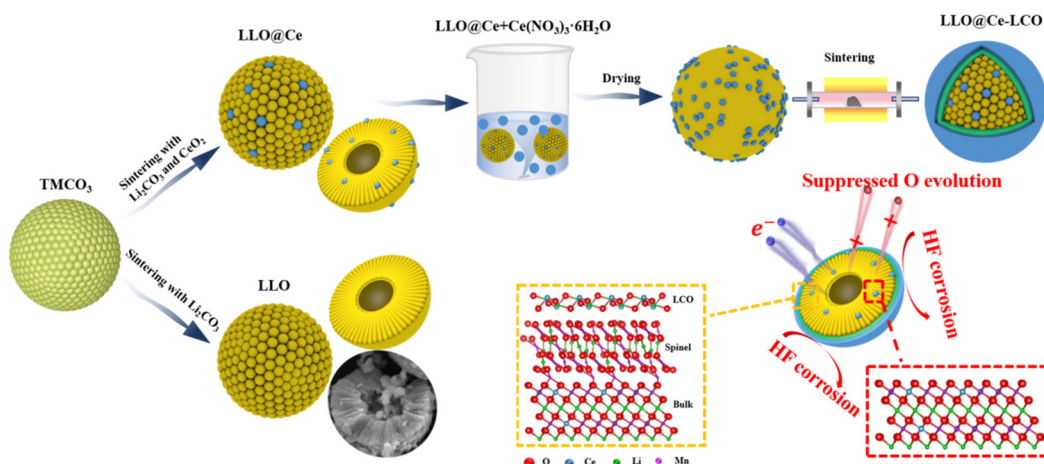
Fig. 1 Schematic diagram of the preparation process and advantages of the LLO@Ce–LCO sample.

to reduce the transport path of Li^+ by preparing Li-rich materials with a hollow architecture, which can improve the transfer capacity of the particles, and then improve the cycling stability by doping Zr and surface coating ZrO_2.[25] Unfortunately, ZrO_2 has little effect on the formation of oxygen vacancies, so the cycling stability of the whole material is limited.

In this work, inspired by the advantages of multiple strategies with a synergistic effect, a spinel heterogeneous interface strategy is proposed for the construction of the $LiCeO_2$@spinel@layered interface after Ce-pre-embedment in the LLO hollow architecture (LLO@Ce–LCO) (in Fig. 1). The elaborately designed LLO@Ce–LCO cathode material with a hollow architecture possesses the following merits. Firstly, LLO@Ce–LCO has a short Li-ion diffusion path owing to its hollow architecture, which is beneficial for Li^+ transport.[26] Secondly, LLO@Ce–LCO exhibits the advantages of high capacity retention due to the surface modification of $LiCeO_2$, which has abundant oxygen vacancies and is beneficial for suppressing the undesired side reactions between the electrode and the electrolyte during the cycle. Thirdly, the spinel phase induced in the subsurface has a three-dimensional transport channel, which is favorable for Li^+ diffusion. Finally, the addition of high-valence Ce ions reduces the average valence state of TM–O, effectively stabilizing the inner anionic oxygen and suppressing transition metal migration. Consequently, the prepared LLO@Ce–LCO delivers a high reversible capacity, remarkable cycling stability, good rate capacity and enhanced voltage retention. The specific capacity of LLO@Ce–LCO is 220 mA h g^{-1} at 1C and remains as high as 189 mA h g^{-1} after 200 cycles.

2. Experimental

2.1. Materials preparation

The $Mn_{0.75}Ni_{0.25}CO_3$ precursor was synthesized using a carbonate coprecipitation method (the detailed method is in the ESI†).

LLO samples were prepared by mixing $Mn_{0.75}Ni_{0.25}CO_3$ precursors and Li_2CO_3 at a molar ratio of Li : TM = 1.05 (Li excess 5%). After calcining at 850 °C for 12 h, the samples were cooled to 500 °C and then sintered at 500 °C for 5 hours under an air atmosphere. LLO@Ce samples were prepared by homogeneously mixing $Mn_{0.75}Ni_{0.25}CO_3$ precursors, Li_2CO_3 and CeO_2 in a molar ratio of Li : TM : Ce = 1.05 : 1 : 0.005, and then sintering according to the above process. For the synthesis of LLO@Ce–LCO, LLO@Ce and $Ce(NO_3)_3 \cdot 6H_2O$ were mixed in an ethanol solution with a molar ratio of TM : Ce = 1 : 0.005, and the desired powder materials were obtained by evaporation by stirring at 80 °C and then calcining at 600 °C for 10 h under an air atmosphere. The synthesis process is shown in Fig. 1.

2.2. Electrochemical measurements

The electrode was prepared by casting a slurry composed of the cathode material, carbon black, and binder (80 : 10 : 10 by weight) on the Al foil to prepare the CR2016 cell. The loading mass of the active material was fixed at 1.0 ± 0.1 mg to ensure the veracity of measurement results. The electrolyte was 1 M $LiPF_6$ in EC/DMC (1 : 1 by volume). The as-prepared cells were subjected to electrochemical measurements *via* Neware software. At room temperature, the charging and discharging range of the battery is 2–4.8 V.

3. Results and discussion

The particle cross-section of LLOs shows that the LLO produced by mixing the LLO precursor and lithium carbonate directly presents a hollow structure (see the SEM illustration in Fig. 1). In order to construct a $LiCeO_2$@spinel@layered interface, the Ce-doped LLO (LLO@Ce) was thoroughly mixed with $Ce(NO_3)_3 \cdot 6H_2O$ solution. After the solution evaporated, Ce elements were gradually deposited on the hollow architecture surface of LLO@Ce. The deposited Ce ions reacted with the Li ions on the LLO@Ce surface during the calcination process to form an epitaxial $LiCeO_2$ coating.[27] The LLO@Ce–LCO main-

tained a typical layered structure, while the $LiCeO_2$ structure (PDF #29-0801) was uniformly formed on the surface, which provided a good abundance of oxygen vacancies, suppressed the redox activity of anionic oxygen and Mn-ion migration, and ultimately improved the electrochemical properties.[28] The XPS spectra of O 1s (Fig. 3e) and the initial charging/discharging profiles (Fig. 4a) of the three samples further confirmed these results. Fig. S1† shows the morphology of the carbonate precursor which is composed of smooth surface microspheres. After calcination at high temperatures, the morphologies of all as-prepared samples show no obvious differences and their average particle size is around 11–15 μm (Fig. 2a–c). Moreover, each element (Mn, Ni and O) is evenly distributed, and Ce has been successfully introduced into the LLO@Ce and LLO@Ce–LCO materials (see the illustration in Fig. 2a–c and Fig. S2†).

Fig. 2d–f displays the TEM images of a pristine LLO and a modified LLO, respectively. The pristine LLO shows a good crystal structure with distinct lattice fringes whose interlayer spacing is 0.470 nm corresponding to the (003) crystal plane of

the Li_2MnO_3 phase (Fig. 2d1 and d2).[29] In contrast, the obvious interplanar spacing lattices in LLO@Ce are increased to 0.478 nm (Fig. 2e1 and e2). Furthermore, the crystal plane spacing of (003) in LLO@Ce–LCO is further increased to 0.484 nm due to the fact that Ce ions induce the spinel structure and surface $LiCeO_2$ coating (Fig. 2f1 and (I)). In addition, significant coating and transition layers can also be observed in Fig. 2f1. The distinct lattice fringe of about 0.471 nm for $Li_4Mn_5O_{12}$ matches the (111) plane (Fig. 2(II)) and that of 0.318 nm for $LiCeO_2$ matches the (111) plane in LLO@Ce–LCO (Fig. 2(III)).[27,30] The LLO@Ce–LCO sample has a weak diffraction peak at about 36.7° by comparing the XRD of the two samples at 36°–38° (Fig. S3a†), which is caused by the $Li_4Mn_5O_{12}$ spinel phase.[11] Additionally, the FFT transformation of the LLO@Ce–LCO sample (Fig. S3b†) shows that the diffraction rings match the (733), (551), (311), (220) and (111) crystal planes of $Li_4Mn_5O_{12}$, respectively, which further demonstrates that the spinel in LLO@Ce–LCO represents the $Li_4Mn_5O_{12}$ phase. These results confirm that the
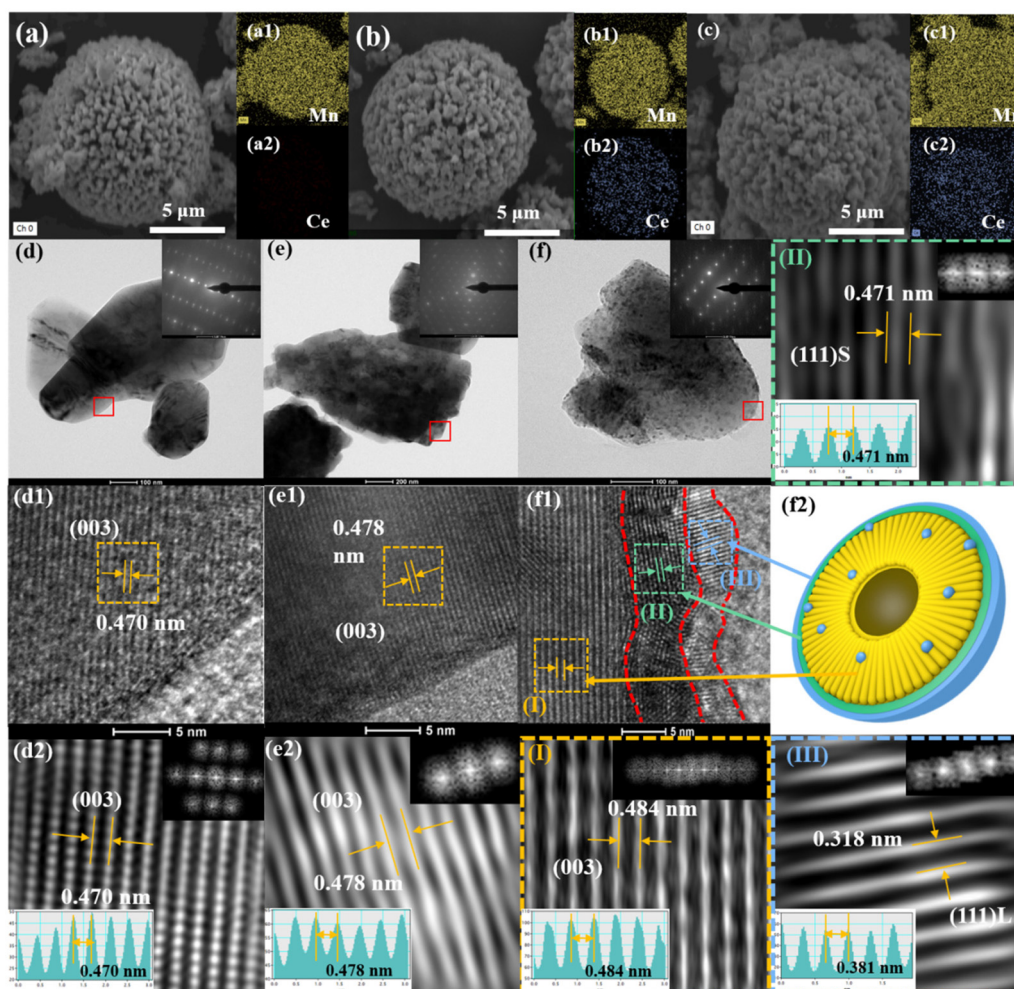

Fig. 2 The SEM and EDS images of (a–a2) LLO, (b–b2) LLO@Ce and (c–c2) LLO@Ce–LCO samples, respectively. The morphologies and lattice structures of (d–d2) LLO, (e–e2) LLO@Ce and (f–f2 and I–III) LLO@Ce–LCO. (d–f) SEM, (d1–f1) HRTEM and SAED images, (d1, d2, e1, e2 and I–III) fast Fourier transform (FFT) and the corresponding line profiles of the Z-contrast information with the measured spacing of TM layers.

LiCeO₂@spinel@layered interface was successfully prepared, and the inner layered structures had not been changed, agreeing with the following X-ray diffraction (XRD) results.

The XRD patterns of a LLO, LLO@Ce and LLO@Ce–LCO are presented in Fig. 3a–c. It can be seen from Fig. 3a–c that all as-prepared samples exhibit similar XRD patterns which have a layered α-NaFeO₂ structure with the space group $R\bar{3}m$.[31] In addition, the few weak peaks appearing between 20° and 25° are characteristic of the monoclinic Li₂MnO₃-like component, which corresponds to the $C2/m$ space group.[32] The XRD patterns of modified LLOs show some unique diffraction peaks from cubic phase CeO₂ (PDF #34-0394) (Fig. 3a). However, the characteristic peak of LCO does not appear in the XRD pattern of the modified samples due to the tiny amount of LCO. Compared with the pristine sample, the angle of the (003) diffraction peak of modified samples has a slight reduction, implying an increase in the cell parameters (a and c), which may be related to the doping of Ce ions into the lattice of the LLO (Fig. 3b). In addition, a clear and distinct splitting diffraction peak of (018)/(110) reveals the well-defined-layered structure (Fig. 3c).[33] The Rietveld refinement of XRD patterns with full spectrum fitting data for three samples was carried out using the GSAS program presented in Fig. S4(a–c) and Tables S1, S2.† Compared with @LLO, the modified LLO shows a long c-axis and a large cell volume, which can be caused by the replacement of the larger radius Ce ions in the lattice. In addition, the modified LLO has lower cation mixing than the pristine LLO by comparing the ratio of I_{003}/I_{104} of the three samples, which is in favour of the rate performance.

XPS was employed to analyze the surface valence and the surface chemistry of three samples (Fig. 3d–g and Fig. S5†). As shown in Fig. 3d, the peaks at 882.1, 888.9 and 898.1 eV and the peaks at 900.2, 907.0 and 916.2 eV are assigned to the Ce $3d_{5/2}$ and Ce $3d_{3/2}$ peaks of Ce⁴⁺ ions, respectively.[34,35] The peaks at 885.4, 897.8 and 903.5 eV belong to Ce³⁺ ions. The existence of Ce⁴⁺ is due to the partial CeO₂ on the surface, which can be seen from XRD results (Fig. 3a). The existence of Ce³⁺ originated from the LiCeO₂ coating, which is consistent with the study reported by Y. T. Ma *et al.*[11] The peaks at 529.4 and 531.5 eV in the O 1s XPS spectra (Fig. 3e) are assigned to lattice oxygen and oxygen vacancies, respectively, verifying that oxygen vacancies increase with the increase in Ce ions. Oxygen vacancies may play a significant part in the storage of oxygen ions, the reduction of oxygen loss and the inhibition of interfacial side reactions. In the Mn 2p region (Fig. 3f), the peak of Mn³⁺ appears in the bulk material after the introduction of Ce, inducing a slight decrease in the average valence state of Mn. The partial oxidation of Mn³⁺ is beneficial for relieving the oxidation degree of lattice oxygen and thus reducing the loss of lattice oxygen in the process of high-voltage charging. In addition, there is no obvious variation of the valence state of Ni before and after modification (Fig. 3g).[36]

The typical charge/discharge curves of the three samples at 0.1C are shown in Fig. 4a, b and Fig. S6.†[37] The first charge curves of the three samples show a slope below 4.5 V and a long plateau region at around 4.5 V. The former corresponds to the Ni-ion oxidation and deintercalation of Li⁺ from LiMO₂ while the latter is ascribed to the electrochemical activation of Li₂MnO₃ accompanied by the irreversible extraction of Li⁺ and the loss of lattice oxygen. During the first three cycles, the capacity of the LLO decreases gradually (Fig. S6a†) while the capacity of the modified LLO has barely decreased, proving
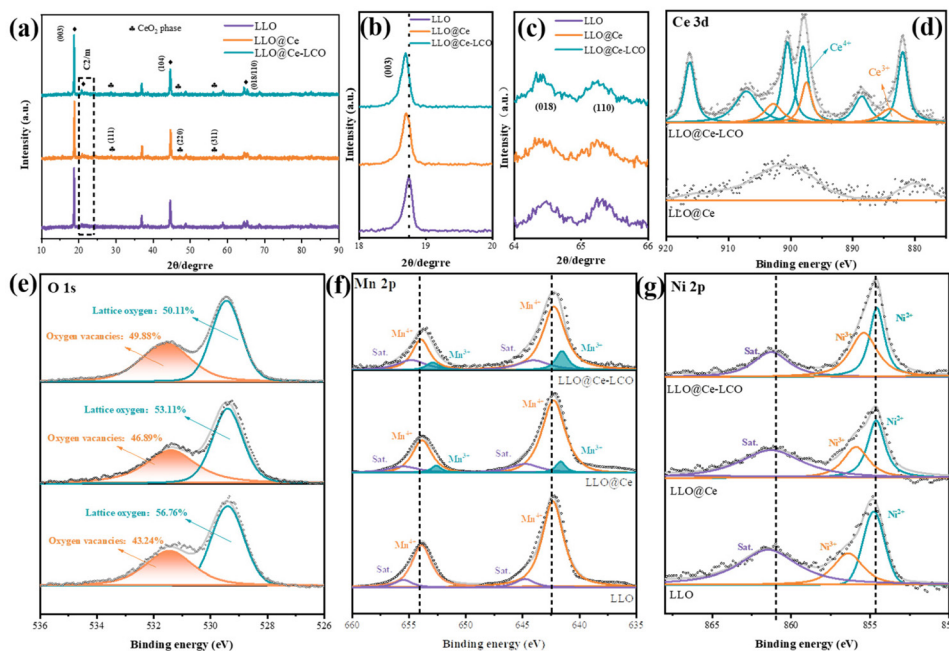

Fig. 3 (a) XRD patterns of the LLO, LLO@Ce and LLO@Ce−LCO samples. (b and c) The enlarged image of the XRD pattern between 18°−20° and 64°−66°. High-resolution XPS spectra of (d) Ce 3d, (e) O 2p, (f) Mn 2p, and (g) Ni 2p for the as-prepared samples.
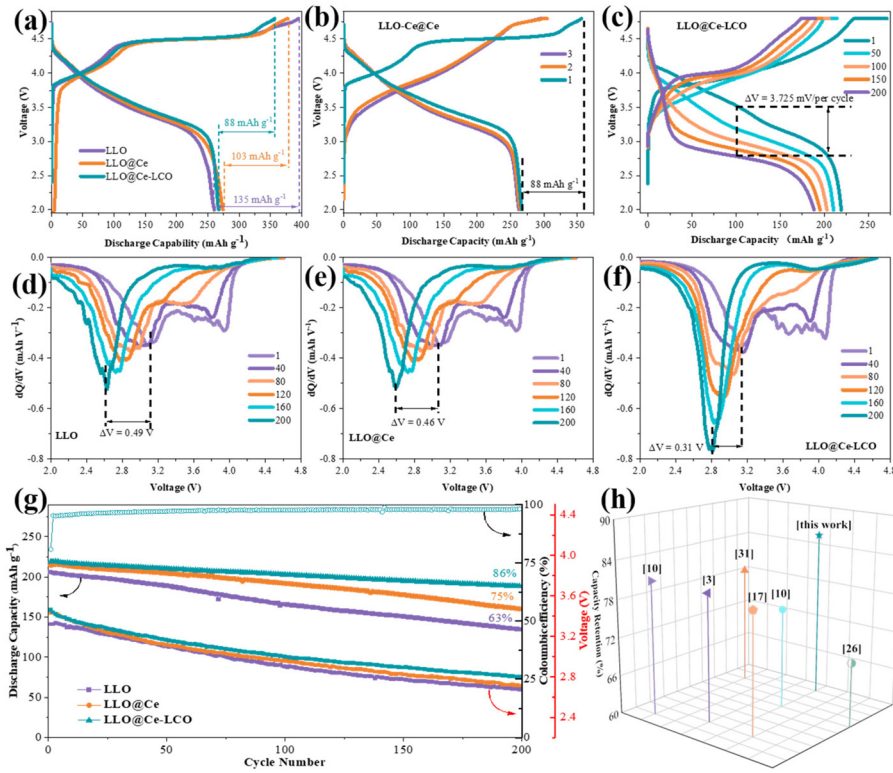
Fig. 4 (a) Initial charging/discharging profiles of the three samples at 0.1C. (b) The first three charge/discharge curves of LLO@Ce−LCO at 0.1C. (c) The voltage profiles of different cycles of LLO@Ce−LCO at 1C. (d−f) The selected differential capacity *versus* voltage curves of the samples at 1C. (g) Cycling performance and Coulombic efficiency of the three samples at 1C. (h) Comparison of the capacity retentions after cycling in our work and other reports.

that the introduction of Ce ions is beneficial for activating the Li$_2$MnO$_3$ phase and keeps the reversible capacity stable. In addition, compared with the pristine LLO in Fig. 4a, the initial Coulomb efficiency (ICE) of the modified LLO is also enhanced by 8–10% due to Ce addition.

Fig. 4c and Fig. S6c, d† present the charge/discharge curves conducted at 1C. The voltage of the three samples obviously decreases with the charging and discharging process going on. The slower the voltage decay, the less harmful the phase transition.[38] In contrast, LLO@Ce−LCO shows the lowest voltage attenuation, demonstrating that LLO@Ce−LCO has a stable lattice structure due to LiCeO$_2$@spinel@layer modification. Additionally, the dQ/dV curves during the charge–discharge process are presented in Fig. 4d–f. Obviously, the transfer of the anodic peaks of LLO@Ce−LCO to a lower voltage is minimal compared with others. The cycling properties of the three samples at 1C are shown in Fig. 4g. The cells are pre-cycled at 0.1C to be activated before charging/discharging at 1C. After 200 cycles, LLO@Ce−LCO shows a higher reversible capacity of 188.5 mA h g^{-1}, corresponding to a capacity retention of 86%, while LLO@Ce and the LLO have reversible capacities of 160.3 and 134.4 mA h g^{-1}, with corresponding capacity retentions of 75% and 63%, respectively. Compared with other modification methods reported in the literature, the lithium-rich materials modified in this work have excellent cycling stability (Fig. 4h and Table S3†). In addition, the

hollow LLO material has better cycling stability and discharge capacity than the LLO solid particles (Fig. S7a†). Additionally, the capacity retention of the LLO@Ce−LCO electrode is close to 82% after 50 cycles at 0.2C (Fig. S7b and c†). These results indicate that the LLO@Ce−LCO material with a sandwich-like configuration (LiCeO$_2$@spinel@layered interface) has better cycling performance than the other two materials. It is worth noting that LLO@Ce−LCO has a voltage decay of 0.67 V over 200 cycles, which is smaller than that of LLO@Ce (0.73 V) and the LLO (0.72 V) (Fig. 4g). Structurally, voltage attenuation mainly results from irreversible phase transformation from the layered to the spinel phase.[39] Hence, LLO@Ce−LCO with less voltage attenuation indicates a more stable structure, resulting in high capacity retention.

The kinetics and stability mechanism were studied in detail to better understand the effectiveness of the surface integrated layer. For electrode kinetics, both the EIS (Fig. 5a and d) and GITT (Fig. 5c and Fig. S8, Table S4†) results indicate the better diffusion of Li-ions into the LLO@Ce−LCO sample with a spinel heterogeneous interface.[40–42] According to the EIS plots, the Warburg diffusion coefficients of the three samples are obtained before and after cycling (Fig. 5b and e). Then, the solid phase diffusion coefficient of Li$^+$ in the material can also be obtained (see the detailed calculation in Fig. S9†).[43] Apparently, LLO@Ce−LCO exhibits the highest Li$^+$ migration coefficient, which is consistent with the rate performance of
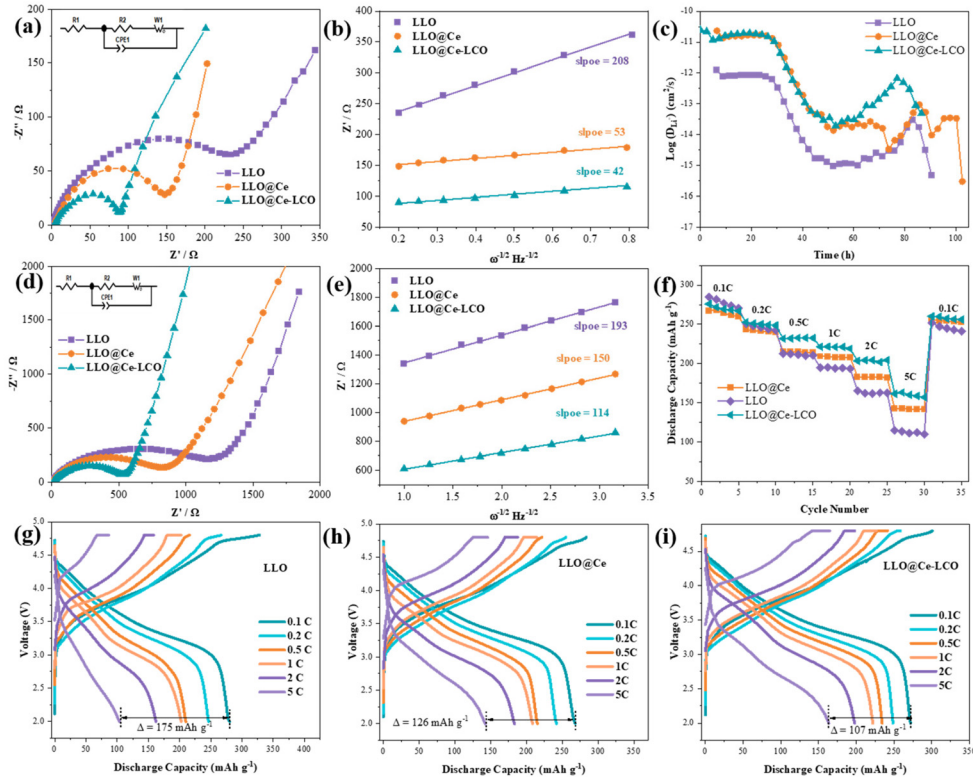
Fig. 5 Nyquist and Z' vs. $\omega^{-1/2}$ plots and Warburg diffusion coefficients of the as-prepared samples before (a and b) and after (d and e) 200 cycles. (c) The calculated Li^+ diffusion coefficients based on Fig. S8.† (f–i) The rate performance and corresponding charge–discharge profiles.

LLO@Ce–LCO (in Fig. 5f). The charge–discharge voltage distributions of the three samples at different current densities are shown in Fig. 5g–i. The smaller gap between the charging and discharging curves of LLO@Ce–LCO indicates that the polarization decreased, in conformity to its distinct spinel heterogeneous interface.[44–46]

The CV curves of the first three cycles of the three samples at a sweep speed of 0.1 mV s[1] were analyzed, as shown in Fig. S10.† The oxidation peak intensity of the LLO@Ce–LCO sample decreased significantly at about 4.6 V, indicating that the oxidation of lattice oxygen is effectively inhibited.[47] Fig. 6 (a–c) presents the CV measurements of the three electrodes at different potential scan rates from 0.1 to 1 mV s[1]. Both the oxidation and reduction peak currents of the three samples increase gradually with the scanning rates shifting toward high and low potentials, respectively.[48,49] As typically shown in Fig. 6(d–f), the shaded area represents the capacitive control process at 0.6 mV s[1] and the corresponding capacitive control ratios of the three samples are 82%, 83% and 92% respectively. As shown in Fig. 6(g), the *b* values of the three samples are 0.74, 0.78 and 0.82, respectively, indicating that the capacity contribution of the LLO electrode is mainly diffusion control, while the capacity of the LLO@Ce–LCO electrode can be regarded as a process in which diffusion control is supplemented and capacitance control is dominant.[50,51] Fig. 6h displays the percentage of the capacitive contribution and diffusion-controlled contribution of the three electrodes. The

three electrodes display similar trends in the capacitive contribution and diffusion-controlled contribution, respectively. However, the capacitive contribution of the LLO@Ce–LCO electrode occupies the dominant position at any scan rate compared with the other electrodes, demonstrating that the enhancement of the rate performance of the LLO@Ce–LCO is ascribed to the improved capacitive effect. A similar phenomenon was also observed in the previous report.[52]

SEM and XPS were employed to further evaluate the structural stability of electrodes at 1C after 200 cycles (Fig. 7). Obviously, severe structural degradation occurs in the LLO (Fig. 7a). The propagation of cracks leads to a decrease in the connectivity of the primary particles, then capacity attenuation and thus failure of the battery. In contrast, LLO@Ce–LCO shows less structural damage, proving the stress buffer effect of multifunctional modification (Fig. 7b). The spectra of both F 1s and O 1s are composed of two peaks, among which the spectra of F 1s are related to $LiF/Li_xPO_yF_z$ (687.5 eV) and C–F (685 eV) (Fig. 7c). The spectra of O 1s are related to TM–O (532 eV) and $ROCO_2Li$ (533 eV) (R represents the alkyl group) (Fig. 7d).[53–55] It is obvious that the TM–O peak of LLO@Ce–LCO is stronger than that of the LLO and LLO@Ce, indicating that TM has less dissolution due to the fact that the $LiCeO_2$ coating layer is not uniformly spread over the surface of the LLO@Ce–LCO sample (Fig. S11†).[27] In addition the weak peak area of $ROCO_2Li$ of LLO@Ce–LCO indicates the suppression of electrolyte decomposition and the formation of a cathode–electrolyte interface
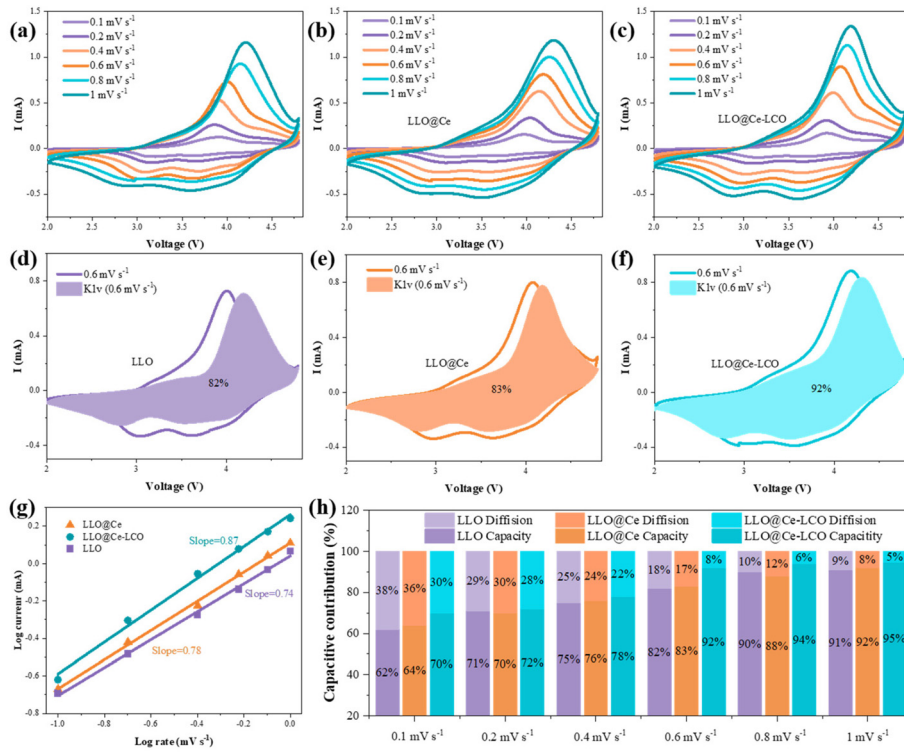
Fig. 6 (a–c) CV curves of the samples at various scan rates from 0.1 to 1 mV s^{-1}. (d–f) Capacitive contribution (shadow area) and diffusion contribution (the rest) to energy storage of three samples at 0.6 mV s^{-1}. (g) Determination of the *b*-values of the as-prepared samples using the relationship between the peak current and the scan rate. (h) Contribution of the surface process in the three electrodes at various scan rates.
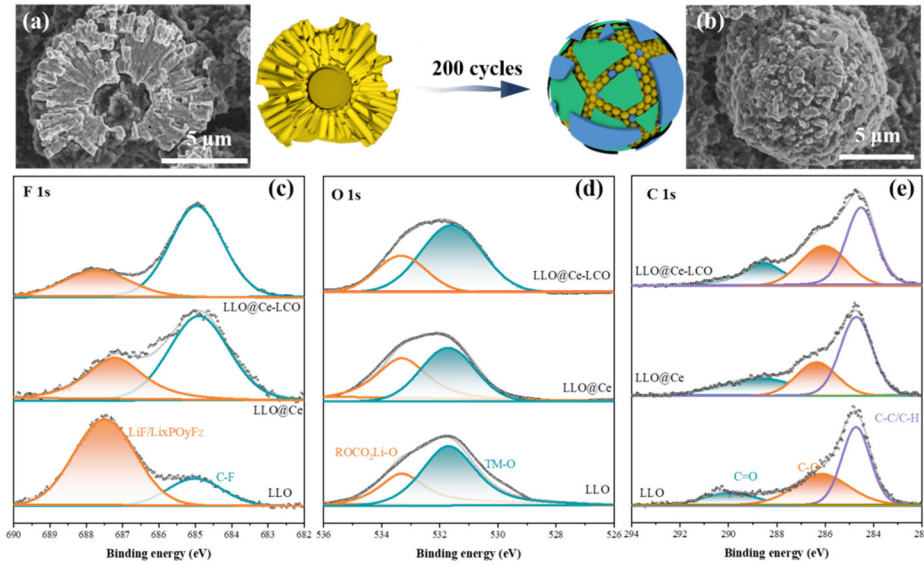

Fig. 7 SEM images of (a) the LLO and (b) LLO@Ce−LCO after 200 cycles at 1C. High-resolution XPS spectra of (c) F 1s, (d) O 1s, and (e) C 1s of the as-prepared samples after 200 cycles.

(CEI). The spectra of C 1s in all electrodes are related to C–C/C–H (284 eV), C–O (288 eV), and C=O (289 eV) (Fig. 7e).[56] The C–C and C–H bonds are involved in the binder and conductive substance, whereas the C–O and C=O bonds originated from the decomposition of carbonate electrolyte solvents. Compared

with the LLO and LLO@Ce, the peak area of the C–O/C=O bonds of LLO@Ce–LCO is smaller, indicating that the CEI film is less formed. Thus, the design of the LLO@Ce–LCO structure plays an important role in maintaining the stability of the overall structure and lattice oxygen evolution, which profits

from the layered structure of Ce ion doping, the spinel structure with advantageous lithium ion transmission paths and the LCO coating with oxygen vacancies.

4. Conclusions

In summary, a spinel heterogeneous interface with oxygen buffering effects has been introduced into the $Li_{1.2}Mn_{0.6}Ni_{0.2}O_2$ hollow architecture by a facile strategy, which can achieve high cycling performance effectively. The particles with a hollow architecture have a short diffusion path, the LCO coating layer can suppress the side reactions between the electrode and the electrolyte, the spinel structure can provide a three-dimensional transport channel for lithium ions and Ce doping can support the structure and lower the TM–O covalency, which can effectively stabilize the inner anionic oxygen and suppress transition metal migration. As a result, the prepared LLO@Ce–LCO undergoes 200 cycles with a high specific capacity of 189 mA h g^{-1}, a high capacity retention of about 86% and a high voltage retention of 81% at 1C. This work provides an easily scalable approach for developing layered cathode materials with excellent cycling stability for next generation lithium ion batteries.

Conflicts of interest

The authors declare that they have no known competing financial interests or personal relationships that could have appeared to influence the work reported in this paper.

Acknowledgements

References

1 S. Kim, W. Cho, X. Zhang, Y. Oshima and J. Choi, A stable lithium-rich surface structure for lithium-rich layered cathode materials, *Nat. Commun.*, 2016, **7**, 13598.

2 K. Nakayama, R. Ishikawa, S. Kobayashi, N. Shibata and Y. Ikuhara, Dislocation and oxygen-release driven delithiation in Li_2MnO_3, *Nat. Commun.*, 2020, **11**, 1–7.

3 Z. Lin, X. Ding, D. Luo, J. Cui, H. Xie and Q. Ren, Ultralong life Li-rich $Li_{1.2}Mn_{0.6}Ni_{0.2}O_2$ cathode by three-in-one surface modification for lithium-ion batteries, *Angew. Chem.*, 2020, **132**, 7852–7856.

4 W. Huang, Q. Liu, Y. Yang, Z. W. Zhou, Y. S. Li, Y. J. Lin, Y. Wang, Y. C. Tu, B. B. Wang, X. H. Zhou, D. H. Deng, B. Yang, Y. Yang, Z. Liu, X. H. Bao and F. Yang, Tuning the activities of cuprous oxide nanostructures via the oxide-metal interaction, *Nat. Commun.*, 2020, **11**, 2312.

5 S. Zhu and J. Chen, Dual strategy with Li-ion solvation and solid electrolyte interphase for high Coulombic efficiency of lithium metal anode, *Energy Storage Mater.*, 2022, **44**, 48–56.

6 Y. Lee, J. Shin, H. Kang, D. Lee, T. Kim, Y. Kwon and E. Cho, Promoting the reversible oxygen redox reaction of Li-excess layered cathode materials with surface vanadium cation doping, *Adv. Sci.*, 2021, **8**, 2003013.

7 W. He, P. Liu, B. Qu, Z. M. Zheng, H. F. Zheng, P. Deng, P. Li, S. Y. Li, H. Huang, L. Wang, Q. S. Xie and D. L. Peng, Uniform Na$^+$ doping-induced defects in Li- and Mn-rich cathodes for high-performance lithium-ion batteries, *Adv. Sci.*, 2019, **6**, 1802114.

8 B. Xiao, H. S. Liu, N. Chen, M. N. Banis, H. J. Yu, J. W. Liang, Q. Sun, T. K. Sham, R. Li, M. Cai, G. Botton and X. L. Sun, Size-mediated recurring spinel sub-nanodomains in Li- and Mn-rich layered cathode materials, *Angew. Chem., Int. Ed.*, 2020, **59**, 14313–14320.

9 L. G. Wang, A. Dai, W. Q. Xu, S. Lee, W. Cha, R. Harder, T. C. Liu, Y. Ren, G. P. Yin and P. J. Zuo, Structural distortion induced by manganese activation in a lithium-rich layered cathode, *J. Am. Chem. Soc.*, 2020, **142**, 14966–14973.

10 Y. Liu, Z. Yang, J. Zhong, J. L. Li, R. R. Li, Y. Yu and F. Y. Kang, Surface-functionalized coating for lithium-rich cathode material to achieve ultra-high rate and excellent cycle performance, *ACS Nano*, 2019, **13**, 11891–11900.

11 Y. T. Ma, P. F. Liu, Q. S. Xie, G. B. Zhang, H. F. Zheng, Y. X. Cai, Z. Li, L. S. Wang, Z. Z. Zhu, L. Q. Mai and D. L. Peng, Double-shell Li-rich layered oxide hollow microspheres with sandwich-like carbon@spinel@layered@spinel@carbon shells as high-rate lithium ion battery cathode, *Nano Energy*, 2019, **59**, 184–196.

12 H. X. Wei, Y. D. Huang, L. B. Tang, C. Yan, Z. J. He, J. Mao, K. H. Dai, X. W. Xu, J. B. Jiang and J. C. Zheng, Lithium-rich manganese-based cathode materials with highly stable lattice and surface enabled by perovskite-type phase-compatible layer, *Nano Energy*, 2021, **88**, 106288.

13 X. Ding, Y. X. Li, S. Wang, J. M. Dong, A. Yasmin, Q. Hu, Z. Y. Wen and C. H. Chen, Towards improved structural stability and electrochemical properties of a Li-rich material by a strategy of double gradient surface modification, *Nano Energy*, 2019, **61**, 411–419.

14 W. Zhu, Z. G. Tai, C. Y. Shu, S. K. Chong, S. W. Guo, L. J. Ji, Y. Z. Chen and Y. N. Liu, The superior electrochemical

performance of a Li-rich layered cathode material with Li-rich spinel $Li_4Mn_5O_{12}$ and MgF_2 double surface modifications, *J. Mater. Chem. A*, 2020, **8**, 7991.

15 Z. W. Zhou, Z. Y. Luo, Z. J. He, J. C. Zheng, Y. J. Li, C. Yan and J. Mao, Suppress voltage decay of lithium-rich materials by coating layers with different crystalline states, *J. Energy Chem.*, 2021, **60**, 591–598.

16 H. F. Zheng, Z. Y. Hu, P. F. Liu, W. J. Xu, Q. S. Xie, W. He, Q. Luo, L. S. Wang, D. D. Gu, B. H. Qu, Z. Z. Zhu and D. L. Peng, Surface Ni-rich engineering towards highly stable $Li_{1.2}Mn_{0.54}Ni_{0.13}Co_{0.13}O_2$ cathode materials, *Energy Storage Mater.*, 2020, **25**, 76–85.

17 F. Wu, W. K. Li, L. Chen, J. Wang, W. Bao, Y. Lu, J. Tan, S. Chen, R. J. Chen and Y. F. Su, Role of $LaNiO_3$ in suppressing voltage decay of layered lithium-rich cathode materials, *J. Power Sources*, 2021, **499**, 229967.

18 H. F. Shang, F. H. Ning, B. Li, Y. X. Zuo, S. G. Lu and D. G. Xia, Suppressing voltage decay of a lithium-rich cathode material by surface enrichment with atomic ruthenium, *ACS Appl. Mater. Interfaces*, 2021, **499**, 229915.

19 J. C. Yang, Y. X. Chen, Y. J. Li, X. M. Xi, J. C. Zheng, Y. L. Zhu, Y. K. Xiong and S. W. Liu, Encouraging voltage stability upon long cycling of Li-rich Mn-based cathode materials by Ta–Mo dual doping, *ACS Appl. Mater. Interfaces*, 2021, **13**, 25981–25992.

20 X. Wu, X. Xiong, B. Yuan, J. Liu and R. Hu, Understanding the phenomenon of capacity increasing along cycles: In the case of an ultralong-life and high-rate SnSe–Mo–C anode for lithium storage, *J. Energy Chem.*, 2022, **72**, 133–142.

21 Y. Yang, J. X. Huang, Z. M. Cao, Z. H. Lv, D. Z. Wu, Z. P. Wen, W. W. Meng, J. Zeng, C. C. Li and J. B. Zhao, Synchronous manipulation of ion and electron transfer in Wadsley–Roth phase Ti–Nb oxides for fast-charging lithium-ion batteries, *Adv. Sci.*, 2022, **9**, 2104530.

22 F. Wan, L. L. Zhang, X. Dai, X. Y. Wang, Z. Q. Niu and J. Chen, Aqueous rechargeable zinc/sodium vanadate batteries with enhanced performance from simultaneous insertion of dual carriers, *Nat. Commun.*, 2018, **9**, 1656.

23 T. Yuan, S. N. Luo, L. K. Soule, J. H. Wang, Y. C. Wang, D. W. Sun, B. T. Zhao, W. W. Li, J. H. Yang, S. Y. Zheng and M. L. Liu, A hierarchical $Ti_2Nb_{10}O_{29}$ composite electrode for high-power lithium-ion batteries and capacitors, *Mater. Today*, 2021, **45**, 8–19.

24 J. Mei, Y. Chen, W. Xu, W. He, L. Wang, Q. S. Xie and D. L. Peng, Multi-strategy synergistic Li-rich layered oxides with fluorine-doping and surface coating of oxygen vacancy bearing CeO_2 to achieve excellent cycling stability, *Chem. Eng. J.*, 2021, **431**, 133799.

25 R. H. Wang, Y. L. Sun, K. S. Yang, J. C. Zheng, Y. Li, Z. F. Qian, Z. J. He and S. K. Zhong, One-time sintering process to modify $xLi_2MnO_3 \cdot (1−x)LiMO_2$ hollow architecture and studying their enhanced electrochemical performances, *J. Energy Chem.*, 2020, **50**, 271–279.

26 Z. J. He, Z. X. Wang, Z. M. Huang, H. Chen and H. J. Guo, A novel architecture designed for lithium rich layered $LiLi_{0.2}Mn_{0.54}Ni_{0.13}Co_{0.13}O_2$ oxides for lithium-ion batteries, *J. Mater. Chem. A*, 2015, **3**, 16817–16823.

27 Y. Y. Liu, Z. Yang, J. J. Zhong, J. L. Li, R. R. Li, Y. Yu and F. Y. Kang, Surface-functionalized coating for lithium-rich cathode material to achieve ultra-high rate and excellent cycle performance, *ACS Nano*, 2019, **13**, 11891–11900.

28 Q. Wang, W. He, L. S. Wang, S. Li, H. F. Zheng, Q. Liu, Y. X. Cai, J. Lin, Q. S. Xie and D. L. Peng, Morphology control and Na^+ doping toward high-performance Li-rich layered cathode materials for lithium-ion batteries, *ACS Sustainable Chem. Eng.*, 2021, **9**, 197–206.

29 Z. Zhu, R. Gao, I. Waluyo, Y. H. Dong, A. Hunt, J. Lee and J. Li, Stabilized Co-free Li-rich oxide cathode particles with an artificial surface prereconstruction, *Adv. Energy Mater.*, 2020, **10**, 2001120.

30 J. Chen, G. Q. Zou, W. T. Deng, Z. D. Huang, X. Gao, C. Liu, S. Y. Yin, H. Q. Liu, X. L. Deng, Y. Tian, J. Y. Li, C. W. Wang, D. Wang, H. W. Wu, L. Yang, H. S. Hou and X. B. Ji, Pseudo-bonding and electric-field harmony for Li-rich Mn-based oxide cathode, *Adv. Funct. Mater.*, 2020, **30**, 2004302.

31 Z. J. He, J. Y. Li, Z. Y. Luo, Z. W. Zhou, X. K. Jiang, J. C. Zheng, Y. J. Li, J. Mao, K. H. Dai, C. Yan and Z. M. Sun, Enhancing cell performance of lithium-rich manganese-based materials via tailoring crystalline states of a coating layer, *ACS Appl. Mater. Interfaces*, 2021, **13**, 49390–49401.

32 J. P. Pender, G. Jha, D. H. Youn, J. M. Ziegler, I. Andoni, E. J. Choi, A. Heller, B. S. Dunn, P. S. Weiss, R. M. Penner and C. B. Mullins, Electrode degradation in lithium-ion batteries, *ACS Nano*, 2020, **14**, 1243–1295.

33 X. Ding, Y. X. Li, X. D. He, J. Y. Liao, Q. Hu, F. Chen, X. Q. Zhang, Y. Zhao and C. H. Chen, Surface $Li^{(+)}/K^{(+)}$ exchange toward double-gradient modification of layered Li-rich cathode materials, *ACS Appl. Mater. Interfaces*, 2019, **11**, 31477–31483.

34 Z. Z. Yu, K. Z. Yu, J. X. Wei, Q. Lu, Y. Cheng and Z. L. Pan, Improves electrode properties by sputtering Ge on SiO anode surface, *Ceram. Int.*, 2022, **48**, 26784–26790.

35 D. Luo, H. X. Xie, F. L. Tan, J. X. Cui, X. Y. Xie, C. Y. Li and Z. Lin, Scalable nitrate treatment for constructing integrated surface structures to mitigate capacity fading and voltage decay of Li-rich layered oxides, *Angew. Chem., Int. Ed.*, 2022, **5**, e202203698.

36 Q. X. Ma, Z. J. Chen, S. W. Zhong, J. X. Meng, F. L. Lai, Z. F. Li, C. Cheng, L. Zhang and T. F. Liu, Na-substitution induced oxygen vacancy achieving high transition metal capacity in commercial Li-rich cathode, *Nano Energy*, 2021, **81**, 105622.

37 C. Cui, X. Fan, X. Zhou, J. Chen and C. Wang, Structure and interface design enable stable Li-rich cathode, *J. Am. Chem. Soc.*, 2020, **142**, 8918–8927.

38 Y. C. Liu, J. Wang, J. W. Wu, Z. Y. Ding, P. H. Yao, S. L. Zhang and Y. N. Chen, 3D Cube-maze-like Li-rich layered cathodes assembled from 2D porous nanosheets

for enhanced cycle stability and rate capability of lithium-ion batteries, *Adv. Energy Mater.*, 2019, **10**, 1903139.

39 J. Hwang, S. Myeong, W. Jin, H. Jang, G. Nam, M. Yoon, S. H. Kim, S. H. Joo, S. K. Kwak, M. G. Kim and J. Cho, Excess-Li localization triggers chemical irreversibility in Li-and Mn-rich layered oxides, *Adv. Mater.*, 2020, **32**, 2001944.

40 Z. Z. Yu, Q. L. Tong, G. Q. Zhao, G. S. Zhu, B. B. Tian and Y. Cheng, Combining surface holistic Ge coating and sub-surface Mg doping to enhance the electrochemical performance of $LiNi_{0.8}Co_{0.1}Mn_{0.1}O_2$ cathodes, *ACS Appl. Mater. Interfaces*, 2022, **14**, 25490–25500.

41 J. S. Yang, P. Li, F. P. Zhong, X. M. Feng, W. H. Chen, X. P. Ai, H. X. Yang, D. G. Xia and Y. L. Cao, Suppressing voltage fading of Li-rich oxide cathode via building a well-protected and partially-protonated surface by polyacrylic acid binder for cycle-stable Li-ion batteries, *Adv. Energy Mater.*, 2020, **10**, 1904264.

42 X. Cao, H. Li, Y. Qiao, M. Jia, X. Li, J. Cabana and H. S. Zhou, Stabilizing anionic redox chemistry in a Mn-based layered oxide cathode constructed by Li-deficient pristine state, *Adv. Mater.*, 2021, **33**, 2004280.

43 W. Zhang, Y. G. Sun, H. Q. Deng, J. M. Ma, Y. Zeng, Z. Q. Zhu, Z. S. Lv, H. R. Xia, X. Ge, S. K. Cao, Y. Xiao, S. B. Xi, Y. H. Du, A. M. Cao and X. D. Chen, Dielectric polarization in inverse spinel-structured Mg_2TiO_4 coating to suppress oxygen evolution of Li-rich cathode materials, *Adv. Mater.*, 2020, **32**, 2000496.

44 Q. Liu, T. Xie, Q. S. Xie, W. He, Y. G. Zhang, H. F. Zheng, X. J. Lu, W. S. Wei, B. S. Sa, L. S. Wang and D. L. Peng, Multiscale deficiency integration by Na-rich engineering for high-stability Li-rich layered oxide cathodes, *ACS Appl. Mater. Interfaces*, 2021, **13**, 8239–8248.

45 J. Wu, X. F. Zhang, S. Y. Zheng, H. D. Liu, J. P. Wu, R. Q. Fu, Y. X. Li, Y. X. Xiang, R. Liu, W. H. Zuo, Z. H. Cui, Q. H. Wu, S. Q. Wu, Z. H. Chen, P. Liu, W. L. Yang and Y. Yang, Tuning oxygen redox reaction through the inductive effect with proton insertion in Li-rich oxides, *ACS Appl. Mater. Interfaces*, 2020, **12**, 7277–7284.

46 Z. Z. Yu, L. H. Zhou, Y. Cheng, K. Wei, G. Qu, N. Hussain, D. Y. Fan, Z. L. Pan and B. B. Tian, Preset lithium source electrolyte boosts SiO anode performance for lithium-ion batteries, *ACS Sustainable Chem. Eng.*, 2022, **10**, 10351–10360.

47 L. Ku, Y. X. Cai, Y. T. Ma, H. F. Zheng, P. F. Liu, Z. S. Qiao, Q. S. Xie, L. S. Wang and D. L. Peng, Enhanced electrochemical performances of layered-spinel heterostructured lithium-rich $Li_{1.2}Ni_{0.13}Co_{0.13}Mn_{0.54}O_2$ cathode materials, *Chem. Eng. J.*, 2019, **370**, 499–507.

48 Y. Cheng, K. Wei, Z. Z. Yu, D. Y. Fan, D. L. Yan, Z. L. Pan and B. B. Tian, Ternary Si–SiO–Al composite films as high-performance anodes for lithium-ion batteries, *ACS Appl. Mater. Interfaces*, 2021, **13**, 34447–34456.

49 Y. J. Niu, Z. Z. Yu, Y. J. Zhou, J. W. Tang, M. X. Li, Z. C. Zhuang, Y. Yang, X. Huang and B. B. Tian, Constructing stable Li-solid electrolyte interphase to achieve dendrites-free solid-state battery: A nano-interlayer/Li pre-reduction strategy, *Nano Res.*, 2022, **18**, 26784–26790.

50 Q. Wang, T. Meng, Y. Li, J. Yang and Y. Tong, Consecutive chemical bonds reconstructing surface structure of silicon anode for high-performance lithium-ion battery, *Energy Storage Mater.*, 2021, **39**, 354–364.

51 C. Liao and S. Wu, Pseudocapacitance behavior on Fe_3O_4-pillared SiO_x microsphere wrapped by graphene as high performance anodes for lithium-ion batteries, *Chem. Eng. J.*, 2019, **355**, 805–814.

52 K. Zhou, Y. N. Li, S. Y. Zhen, M. J. Zhang, C. Y. Zhang, C. Battaglia, H. D. Liu, K. Wang, P. F. Yan, J. J. Liu and Y. Yang, Tailoring the redox-active transition metal content to enhance cycling stability in cation-disordered rock-salt oxides, *Energy Storage Mater.*, 2021, **43**, 275–283.

53 Y. Su, M. Wang, Y. Han, L. Chen and B. Huang, Facile oxidant-assisted treatment to improve the cyclic performance of Li-rich cathode materials, *J. Alloys Compd.*, 2021, **883**, 160814.

54 C. L. Jiao, X. J. Song, X. Q. Zhang, L. X. Sun and H. Q. Jiang, MOF-mediated interfacial polymerization to fabricate polyamide membranes with a homogeneous nanoscale striped turing structure for CO_2/CH_4 separation, *ACS Appl. Mater. Interfaces*, 2021, **13**, 18380–18388.

55 K. H. Hu, L. Ren, W. F. Fan, B. Zhang, M. H. Zuo, Y. H. Zhang, G. P. Lv, H. Y. Xu, W. Xiang and X. D. Guo, *J. Energy Chem.*, 2022, **71**, 266–276.

56 W. Zhu, Z. G. Tai, C. Y. Shu, S. K. Chong, S. W. Guo, L. J. Ji, Y. Z. Chen and Y. N. Liu, The superior electrochemical performance of a Li-rich layered cathode material with Li-rich spinel $Li_4Mn_5O_{12}$ and MgF_2 double surface modifications, *J. Mater. Chem. A*, 2020, **8**, 7991–8001.